Chinese Chemical Letters 31 (2020) 2305–2308

Contents lists available at ScienceDirect

Chinese Chemical Letters

journal homepage: www.elsevier.com/locate/cclet

Communication

3D crumbled MXene for high-performance supercapacitors

Xin Zhang, Jiawei Miao, Peng Zhang, Qizhen Zhu*, Mingchi Jiang, Bin Xu*

State Key Laboratory of Organic–Inorganic Composites, Beijing Key Laboratory of Electrochemical Process and Technology for Materials, Beijing University of Chemical Technology, Beijing 100029, China

ARTICLE INFO

Article history:
Received 4 March 2020
Received in revised form 12 March 2020
Accepted 13 March 2020
Available online 19 March 2020

Keywords:
Supercapacitors
MXene nanosheets
3D porous structure
Capacitance
Rate performance

ABSTRACT

MXene materials have recently attracted considerable attention in energy storage application owing to their metallic conductivity, 2D structure and tunable surface terminations. However, the restacking of 2D MXene nanosheets hinders the ion transport and accessibility to the surface, resulting in adverse effect on their electrochemical performances. Here, with the assistance of hexamethylenetetramine ($C_6H_{12}N_4$), 2D $Ti_3C_2T_x$ MXene nanosheets were fabricated into a 3D architecture with crumbled and porous structure through an electrostatic self-assembly followed by annealing. The resultant 3D structure can expose massive active sites and facilitates the ion transport, which is beneficial for sufficient utilization of the outstanding superiorities of the MXene. Therefore, as a pseudocapacitive material, the 3D crumpled and porous $Ti_3C_2T_x$ MXene shows a gravimetric capacitance of 333 F/g at 1 A/g, and maintains 261 F/g and 132 F/g at ultrahigh current densities of 100 A/g and 1000 A/g, respectively, revealing promising potential for application in supercapacitors.

Supercapacitors are well known as reliable energy storage devices with long cycle life and high power density, but their wide applications are restricted by the relatively low energy density [1]. MXenes, with a general formula of $M_{n+1}X_nT_x$ (M is a transition metal, X is C and/or N, T_x is surface terminations such as −O, −OH, −F), are a new family of 2D materials found in 2011 [2], which show attractive prospect in the field of energy storage [3–10]. Especially, MXenes are very promising electrode materials for supercapacitors because of their metallic conductivity, high capacitance, 2D layered structure and hydrophilic surface together with tunable terminations [11]. However, similar to other 2D materials, the restacking and aggregation of the MXene nanosheets severely limits their performance for energy storage.

To solve this problem, many strategies have been proposed, such as assembling 2D $Ti_3C_2T_x$ MXene sheets into 3D macroscopic structures [12–14], creating porous architectures [15–19] and introducing "spacers" to increase the interlayer spacing [20,21]. Among these strategies, constructing 3D MXene structures can provide massive active sites and interconnected channels for fast ion transport, leading to significantly improved capacitance and rate performance of MXenes. For example, the 3D MXene hydrogel was synthesized *via* a self-assembly approach with the aid of graphene oxide (GO) and ethylenediamine (EDA) [14]. As the EDA reductant promoted the reaction between the epoxy groups on GO and MXene sheets, 3D hybrid hydrogel of MXene and partially reduced GO was formed, which exhibited large capacitance and good rate capability. Another example of 3D porous MXene framework was fabricated with 1D bacterial cellulose (BC) fibers as substrate through freeze-casting and drying method [19]. The 3D MXene/BC film, even with a mass loading of 5 mg/cm^2, possessed ultrahigh capacitance. All these results confirm that the porosity in the 3D MXene framework is very effective to facilitate ion transport and improve the ion accessibility to the active sites.

Here, a 3D porous MXene structure was constructed *via* electrostatic self-assembly of MXene with positively charged hexamethylenetetramine ($C_6H_{12}N_4$) followed by thermal annealing. The 3D MXene provides massive ion-accessible active sites and porous network for fast ion transport together with the shortened ion transport distance. As a result, the 3D MXene, used as an electrode material in supercapacitors, presents high capacitance, superior rate performance 261 F/g at 100 A/g and 132 F/g at 1000 A/g and outstanding cycle stability.

As illustrated in Fig. 1a, the facile assembly of the 3D MXene is proposed as follows: Firstly, the $C_6H_{12}N_4$ was pretreated with HCl solution to be positively charged *via* a protonation reaction. In this process, the amidogen group ($-NH_2$) of $C_6H_{12}N_4$ can get proton (H^+) from HCl solution. Subsequently, the positively charged $C_6H_{12}N_4$ was thoroughly mixed with the $Ti_3C_2T_x$ MXene aqueous suspension. As the MXene nanosheets are negatively charged

* Corresponding authors.
E-mail addresses: zhuqz@mail.buct.edu.cn (Q. Zhu), xubin@mail.buct.edu.cn, binxumail@163.com (B. Xu).

https://doi.org/10.1016/j.cclet.2020.03.040

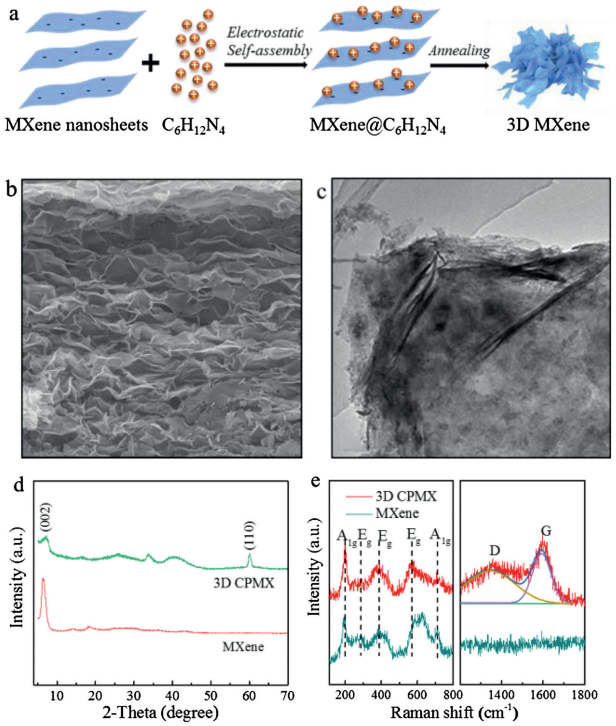

Fig. 1. (a) Schematic illustration of the fabrication process of the 3D CPMX. (b) SEM and (c) TEM images of the 3D CPMX. (d) XRD patterns and (e) Raman spectra of the 3D CPMX and the conventional MXene powder.

owing to the surface terminations, the positively charged $C_6H_{12}N_4$ was electrostatically assembled onto the MXene nanosheets. It is noteworthy that the stability of MXene aqueous suspension is due to the negatively charged hydrophilic surface and the repulsion force between the MXene nanosheets. Thus, during the electrostatic self-assembly, colloidal coagulation occurred [22] and the MXene@$C_6H_{12}N_4$ composites were gradually precipitated. After the thermal annealing treatment at 500 °C under N_2 atmosphere to decompose $C_6H_{12}N_4$, the 3D MXene with crumpled and porous structure was obtained, which was denoted as 3D CPMX.

The morphology of conventional MXene powder and 3D CPMX was compared by SEM and TEM images. The pure MXene shows a dense structure with layer-by-layer stacked sheets (Fig. S1 in Supporting information), while the CPMX exhibits a 3D porous architecture constructed by the highly wrinkled sheets (Fig. 1b). Furthermore, as shown in the TEM image in Fig. S2 (Supporting information), the single-layer MXene nanosheet is almost transparent to the electron beam with no obvious wrinkle, which is ascribed to the flexible and elastic properties of the ultrathin MXene nanosheet [23]. By contrast, the CPMX (Fig. 1c) is obviously more crumbled. XRD is used to further study the structure of the 3D CPMX. As shown in Fig. 1d, the intrinsic (002) peak of MXene can be observed for both MXene powder and 3D CPMX. However, compared with the conventional MXene powder, the (002) peak becomes much broadened for 3D CPMX. Besides, the CPMX shows an additional (110) peak at about 61°. These results imply that the stacked lamellar nanosheets of conventional MXene were disrupted, further confirming the establishment of the 3D structure in CPMX. Also, no characteristic peak of TiO_2 can be observed in both the two samples, indicating the MXene was not oxidized during the fabrication process of the 3D structure.

Fig. 1e shows Raman spectra of the conventional MXene and the 3D CPMX. In the Raman shift range from 100 cm^{-1} to 800 cm^{-1}, the spectra of the 3D CPMX and the conventional MXene are similar. The peaks located at around 197.7, 279.8, 384.9, 580.1 and

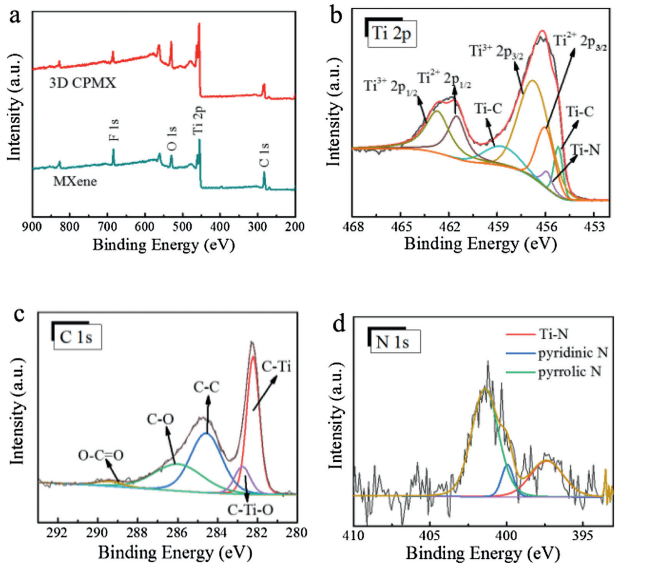

Fig. 2. (a) XPS survey spectra of the 3D CPMX and the conventional MXene powder. (b) Ti 2p, (c) C 1s and (d) N 1s spectra of the 3D CPMX.

713.5 cm^{-1} are related to the specific MXene bands. Among them, the peaks at 197.7 and 713.5 cm^{-1} can be attributed to the A_{1g} vibrational modes of Ti-C, and the peaks at 279.8, 384.9 and 580.1 cm^{-1} result from the E_g group vibrations of Ti-C [24]. Furthermore, two broad bands appear at 1346.2 and 1592 cm^{-1} for the 3D CPMX, corresponding to the characteristic D and G bands of graphitic carbon, respectively. It means the presence of carbon in the 3D CPMX, which may be produced from the decomposition of the $C_6H_{12}N_4$. In addition, the characteristic peak of the anatase phase TiO_2 (usually at 144 cm^{-1}) is not observed in the spectrum of 3D CPMX, demonstrating that no MXene was oxidized during the electrostatic adsorption and thermal decomposition of $C_6H_{12}N_4$.

XPS spectra were employed to investigate the element state of the 3D CPMX and the conventional MXene samples. As shown in Fig. 2a, both the two samples are mainly composed of C, Ti, O, and F elements [25]. The carbon content of the 3D CPMX (43.73 at%) is slightly higher than that of the conventional MXene (41.81 at%), indicating a few residual carbon caused by the decomposed $C_6H_{12}N_4$. The carbon can act as spacer to further open the MXene structure, leading to the further improved capacitive performance. Interestingly, the 3D CPMX also possesses a small amount of N element (1.2 at%), which is probably originated from the thermal decomposition of the $C_6H_{12}N_4$. In the Ti 2p spectrum of the 3D CPMX (Fig. 2b), no TiO_2 peak (458.5 eV) can be seen, verifying no oxidation. Furthermore, compared with the conventional MXene (Fig. S3a in Supporting information), the 3D CPMX exhibits an extra peak at 459.9 eV, which is assigned to Ti-N bonds [20]. Moreover, the C 1s spectra of the 3D CPMX (Fig. 2c) and the conventional MXene (Fig. S3b in Supporting information) show the similar peaks at 282.2, 282.8, 284.6, 286.0 and 289.4 eV, corresponding to C—Ti, C—Ti—O, C—C, C—O and O—C=O bonds, respectively. The N 1s spectrum of the 3D CPMX (Fig. 2d) shows three peaks at 397.4, 399.9, and 401.4 eV, which is ascribed to Ti-N (26.68%), pyridinium (8.47%), and pyrrole nitrogen (64.85%), respectively. It is believed that the nitrogen doping can modify the surface properties, provide high ion accessibility, promote the redox reaction, and enhance the electronic conductivity of MXenes [26,27], although further studies of the influence mechanisms are still needed. Additionally, compared with that of the conventional MXene (Fig. S3c in Supporting information), the O 1s spectrum of the 3D CPMX (Fig. S3d in Supporting information) reveals weaker peak

intensity of Ti−OH at 531.7 eV [28], demonstrating that −OH terminations are partly removed during the thermal treatment.

The electrochemical performances of the 3D CPMX were evaluated by a three-electrode system in 3 mol/L H_2SO_4 electrolyte. The excessive dose of activated carbon and the Ag/AgCl electrode was used as the counter and reference electrodes, respectively. Fig. 3a shows the cyclic voltammetry (CV) curves of the 3D CPMX and the conventional MXene electrodes at a scan rate of 20 mV/s in a potential range of -0.6∼0.3 V (*vs.* Ag/AgCl). Both the two electrodes exhibit distorted curve shape with a pair of broad redox peaks, including the cathodic peaks at about -0.29 V and the anodic peaks at around -0.21 V (*vs.* Ag/AgCl). These redox peaks suggest the pseudocapacitance mechanism on basis of the reversible H^+-involving redox reactions, which is a typical behavior of $Ti_3C_2T_x$ MXene in H_2SO_4 electrolyte [29]. Furthermore, the curve area of the 3D CPMX electrode is much larger than that of the conventional MXene electrode, demonstrating the significantly enhanced capacitance. With the scan rate increasing, the superiority of the 3D CPMX electrode is revealed apparently. As the scan rate increases from 10 mV/s to 500 mV/s, the CV profiles of the 3D CPMX electrode (Fig. 3b) show only a small distortion shape as well as much higher capacitance than the conventional MXene electrode (Fig. 3c).

The galvanostatic charge-discharge curves of the 3D CPMX electrodes at various current densities from 1 A/g to 20 A/g are shown in Fig. 3d. The curves present the almost symmetrical shape with the ultrahigh columbic efficiency of ∼100%. The capacitance of the CPMX electrode reaches as high as 333 F/g at 1 A/g, much higher than that of the conventional MXene (282 F/g). Fig. 3e shows the rate capacitances of the 3D CPMX electrode with the conventional MXene as a comparison. At each current density, the 3D CPMX electrode possesses much higher capacitances than the conventional MXene electrode. The 3D CPMX electrode shows a capacitance of 261 F/g at 100 A/g, almost 1.7 times higher than the conventional MXene electrode 151 F/g at 100 A/g. The 3D CPMX electrode can even endure an ultrahigh current density of 1000 A/g Fig. S4 in Supporting Information with a high capacitance of 132 F/g. Obviously, these high capacitances and excellent rate capability are ascribed to the 3D crumbled and porous structure of the CPMX.

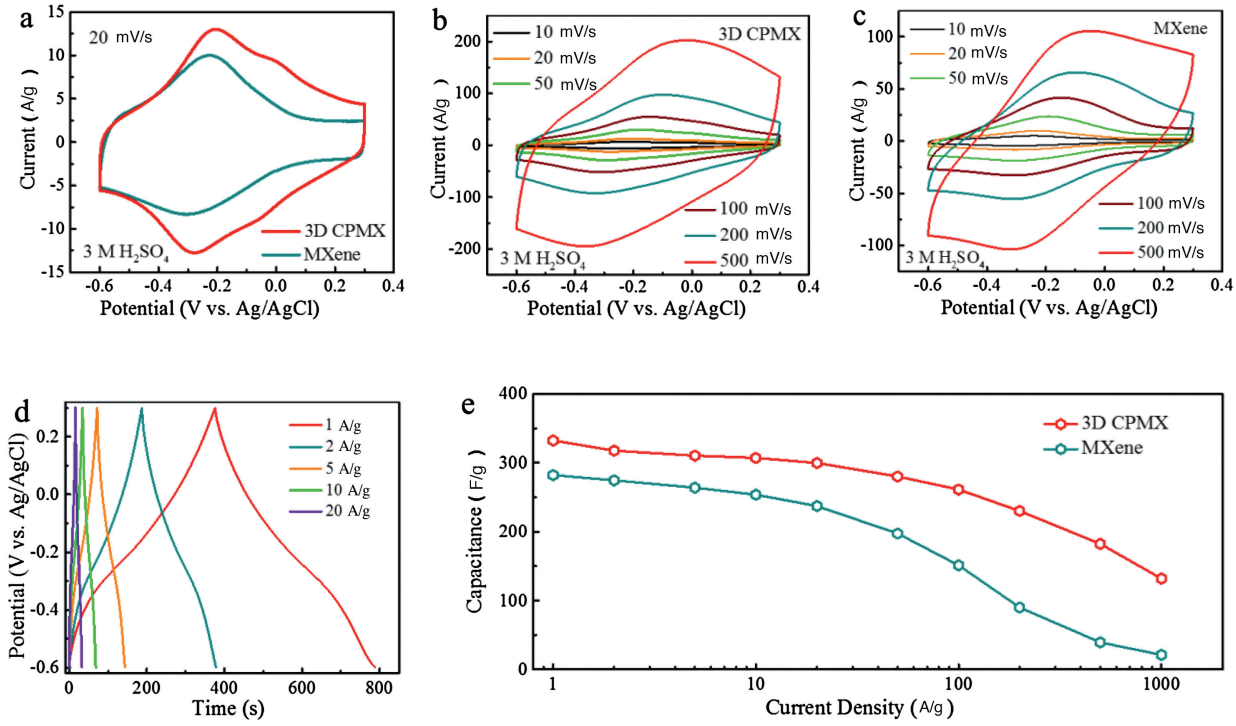

Fig. 3. (a) CV profiles of the 3D CPMX and the conventional MXene electrodes at 20 mV/s. CV profiles at different scan rates of (b) the 3D CPMX and (c) the conventional MXene electrodes. (d) Galvanostatic charge-discharge curves of the 3D CPMX electrodes at various current densities. (e) Rate performance of the 3D CPMX and the conventional MXene electrodes.

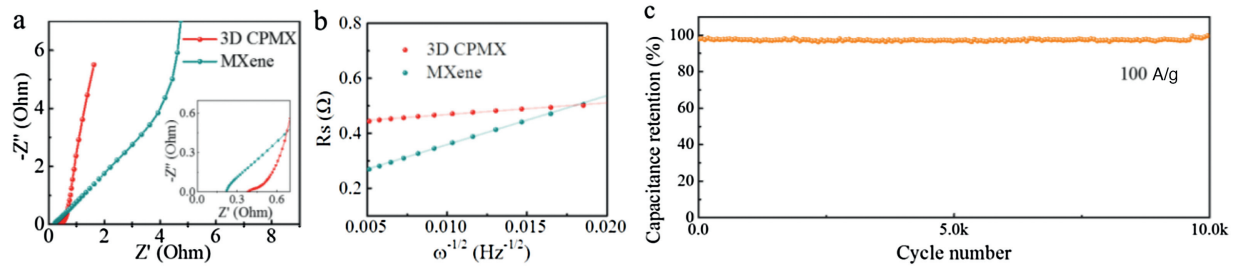

Fig. 4. (a) Nyquist plots of the 3D CPMX and the MXene electrodes. (b) Linear fit of data of Z' against $\omega^{-1/2}$. (c) Cycle performance of the 3D CPMX electrode at 100 A/g for 10,000 cycles.

To clarify the kinetics of the electrochemical process, the Nyquist plots from electrochemical impedance spectroscopy (EIS) of the 3D CPMX and the conventional MXene electrodes are depicted in Fig. 4a. In the low frequency region, the 3D CPMX electrode shows a nearly vertical line, revealing fast ion diffusion and good electrochemical capacitive behavior. Fitted with the equivalent circuit in Fig. S5 (Supporting information), the charge transfer resistance (R_{ct}) of the 3D CPMX and the conventional MXene electrodes are calculated to be 0.03 Ω and 0.08 Ω, respectively. The lower R_{ct} of the CPMX electrode can be attributed to the much larger ion-accessible active surface in the 3D crumpled structure [30]. In addition, from the relationship between Z' data and ω in the high frequency region, as illustrated in Fig.4b, the 3D CPMX electrode exhibits much lower slope of the fitted lines than the conventional MXene electrode. It reflects that the 3D crumbled and porous structure endows the CPMX with fast ion diffusion kinetics. Besides, the long-term cycling stability of the 3D CPMX electrode was evaluated in 3 mol/L H_2SO_4 electrolyte (Fig. 4c). The 3D crumbled porous structure is very stable, ensuring outstanding cycling stability with no capacitance fade during cycling. Furthermore, along with the cycling process, more active sites further expose for ion accessibility due to the activation effect. Therefore, the 3D CPMX delivers a capacitance retention of 101.2% after 10,000 charge-discharge cycles at a current density of 100 A/g.

In summary, the 3D MXene architecture with crumpled and porous structure was synthesized *via* a facile electrostatic self-assembly followed by thermal annealing with the assistance of $C_6H_{12}N_4$. The 3D crumpled and porous MXene framework provides massive ion-accessible active sites and facilitates the fast ion transport. As a result, when used as an electrode material for supercapacitors, the 3D CPMX shows high capacitance, excellent rate capability 261 F/g at 100 A/g, 132 F/g at 1000 A/g, and outstanding cycling performance. These results suggest that the 3D CPMX may be a promising candidate for high-performance supercapacitors.

Declaration of competing interest

The authors declare that they have no known competing financial interests or personal relationships that could have appeared to influence the work reported in this paper.

Acknowledgments

This work was financially supported by the National Natural Science Foundation of China (NSFC, No. 51572011), the National Key Research and Development Program of China (No. 2017YFB0102204) and the Fundamental Research Funds for the Central Universities (Nos. buctrc201813 and buctrc201819).

Appendix A. Supplementary data

Supplementary material related to this article can be found, in the online version, at doi:https://doi.org/10.1016/j.cclet.2020.03.040.

References

[1] N. Jabeen, A. Hussain, Q. Xia, et al., Adv. Mater. 29 (2017) 1700804.
[2] M. Naguib, M. Kurtoglu, V. Presser, et al., Adv. Mater. 23 (2011) 4248–4253.
[3] X. Zhang, L. Wang, W. Liu, et al., ACS Omega 5 (2020) 75–82.
[4] M. Xu, N. Bai, H.X. Li, et al., Chin. Chem. Lett. 29 (2018) 1313–1316.
[5] B. Xu, S. Qi, M. Jin, et al., Chin. Chem. Lett. 30 (2019) 2053–2064.
[6] P. Yu, G. Cao, S. Yi, et al., Nanoscale 10 (2018) 5906–5913.
[7] N. Sun, Q. Zhu, B. Anasori, et al., Adv. Funct. Mater. 29 (2019) 1906282.
[8] L. Yu, L. Hu, B. Anasori, et al., ACS Energy Lett. 3 (2018) 1597–1603.
[9] J.A. Gu, Q. Zhu, Y.Z. Shi, et al., ACS Nano 14 (2020) 891–898.
[10] Q. Zhao, Q. Zhu, J. Miao, et al., Nanoscale 11 (2019) 8442–8448.
[11] D. Pech, M. Brunet, H. Durou, et al., Nat. Nanotechnol. 5 (2010) 651–654.
[12] W. Ma, H. Chen, S. Hou, et al., ACS Appl. Mater. Interfaces 11 (2019) 25369–25377.
[13] Y. Chen, X. Xie, X. Xin, et al., ACS Nano 13 (2019) 295–304.
[14] T. Shang, Z. Lin, C. Qi, et al., Adv. Funct. Mater. 29 (2019) 1903960.
[15] Q. Zhao, Q. Zhu, J. Miao, et al., Small 15 (2019) 1904293.
[16] M.Q. Zhao, X. Xie, C.E. Ren, et al., Adv. Mater. 29 (2017) 1702410.
[17] J. Liu, H.B. Zhang, R. Sun, et al., Adv. Mater. 29 (2017) 1702367.
[18] Z. Ma, X. Zhou, W. Deng, et al., ACS Appl. Mater. Interfaces 10 (2018) 3634–3643.
[19] Y. Wang, X. Wang, X. Li, et al., Adv. Funct. Mater. 29 (2019) 1900326.
[20] J. Li, X. Yuan, C. Lin, et al., Adv. Energy Mater. 7 (2017) 1602725.
[21] H. Chen, L. Yu, Z. Lin, et al., J. Mater. Sci. 55 (2020) 1148–1156.
[22] W. Bao, L. Liu, C. Wang, et al., Adv. Energy Mater. 8 (2018) 1702485.
[23] Y.T. Liu, P. Zhang, N. Sun, et al., Adv. Mater. 30 (2018) 1707334.
[24] J. Yan, C.E. Ren, K. Maleski, et al., Adv. Funct. Mater. 27 (2017) 1701264.
[25] X. Zhang, X. Liu, S. Dong, et al., Appl. Mater. Today 16 (2019) 315–321.
[26] C. Yang, Y. Tang, Y. Tian, et al., Adv. Energy Mater. 8 (2018) 1802087.
[27] L. Yang, W. Zheng, P. Zhang, et al., Electrochim. Acta 300 (2019) 349–356.
[28] J. Ran, G. Gao, F.T. Li, et al., Nat. Commun. 8 (2017) 13907.
[29] Z. Fan, Y. Wang, Z. Xie, et al., Adv. Sci. 5 (2018) 1800750.
[30] M. Ghidiu, M.R. Lukatskaya, M.Q. Zhao, et al., Nature 516 (2014) 78–81.